Optical Gain in AlGaN Quantum Wells: Impact of Higher Energy States

Sebastian Kölle, Friedhard Römer, Giulia Cardinali, Alexander Schulz, Norman Susilo, Daniel Hauer Vidal, Tim Wernicke, Michael Kneissl, *Fellow, IEEE*, and Bernd Witzigmann, *Senior Member, IEEE*

***Abstract*—Simulations of optical gain in aluminum gallium nitride (AlGaN) quantum wells are extended to the high charge carrier density regime required for achieving gain at 275 nm for UV laser diodes. Coulomb interaction is modeled using the 2nd Born approximation. We demonstrate good agreement with experimental data obtained through optical pumping, and predict gain spectra for electrical pumping. Special consideration is given to the contribution of higher bands in wide quantum wells.**

***Index Terms*—Simulation, quantum well lasers, optoelectronic devices, aluminum gallium nitride.**

I. Introduction

As HAS recently been demonstrated [2], aluminum gallium nitride (AlGaN) based laser diodes can achieve continuous wave UV-C lasing at current densities $J > J_{\text{th}} = 4.2$ kA/cm^2.

The high threshold current density J_{th} stems from multiple issues along the lasing process. Carrier transport struggles with injection loss, most notably due to low hole mobility and thus injection [3], [4], [5]. For stimulated emission, only a fraction of the carrier density contributes to gain. Light propagation suffers from optical losses [3], [6]. Investigation and mitigation of these loss mechanisms could pave the road for a new class of UV-C lasers with applications in high-resolution manufacturing (singulation [7], polymerization [8]) and imaging (UV Raman spectroscopy [9], in-vivo fluorescence spectroscopy [10]).

To this end, we provide guidance for the design of future UV-C laser diodes, specifically the quantum well (QW). In the following, we simulate and examine stimulated emission, with a focus on maximizing peak gain.

Gain spectra are simulated for different charge densities and pumping methods. We investigate the impact of QW width, as wide QWs show different transition rates and density of states, which drastically affects the gain spectrum. From there, we analyze the influence of higher energy levels in wide QWs.

width		x_{Al}
10 nm	AlN cap	1
50 nm	waveguide	0.63
d_{QW}	quantum well	x_{QW}
50 nm	waveguide	0.63
900 nm	cladding	0.76
25 nm	buffer transition	⋮
400 nm	buffer	1

Fig. 1. Layers of investigated structures, including Al mole fraction x_{Al}.

The investigated structures consist of $Al_xGa_{1-x}N$ layers epitaxially grown on an AlN/sapphire substrate (see Fig. 1); most notably a 100 nm waveguide with mole fraction $x = 0.63$ in which the QW is embedded. Two different QW designs with width $d_{QW} = 3$ nm and $d_{\text{QW}} = 12$ nm are tested, with $x_{QW} = 43.8\%$ and 42.9% respectively, which were chosen for 275 nm emission.

II. Simulation Model

The simulation process is shown schematically in Fig. 2.

Material parameters are taken from established literature [11], [12], [13], [14], [15], [16].

Gain is derived from microscopic polarization, which is solved using the semiconductor Bloch equations. We apply the $k{\cdot}p$ method, with valence subbands represented in a reduced $k{\cdot}p$ 6×6 basis (HH, LH, CH) i.e. heavy hole, light hole, and crystal-field split-off hole bands [17], [18]. The eigenstates $E_n(k), \psi_n(k,z)$ are derived iteratively as a self-consistent solution to Schrödinger and Poisson equation. This also yields the quasi Fermi levels E_{Fn}, E_{Fp} as a byproduct.

Due to the wurtzite crystal lattice of AlGaN, the strain at QW interfaces causes polarization charges [19]. This induces charge separation between electron and hole states in the QW, leading to lower wavefunction overlap (see Fig. 3) and thus reduced radiative recombination [18]. However, part of these interface charges can be screened by electrons and holes from trap states and external charges [20], which originate from outside the simulated region. In lieu of a full device transport simulation, we model this as a reduction of the effective polarization charge by

Manuscript received 22 January 2024; revised 29 February 2024; accepted 14 March 2024. Date of publication 19 March 2024; date of current version 10 April 2024. This work was supported by the Leibniz Association joint project UVSimTech under Contract K415/2021. *(Corresponding author: Sebastian Kölle.)*

Sebastian Kölle, Friedhard Römer, and Bernd Witzigmann are with the Institute for Optoelectronics, Friedrich-Alexander-Universität Erlangen-Nürnberg, 91052 Erlangen, Germany (e-mail: sebastian.koelle@fau.de).

Giulia Cardinali, Alexander Schulz, Norman Susilo, Daniel Hauer Vidal, and Tim Wernicke are with the Institute of Solid State Physics, Technische Universität Berlin, 10623 Berlin, Germany.

Michael Kneissl is with the Institute of Solid State Physics, Technische Universität Berlin, 10623 Berlin, Germany, and also with the Ferdinand-Braun Institute (FBH), 12489 Berlin, Germany.

Digital Object Identifier 10.1109/JPHOT.2024.3379231

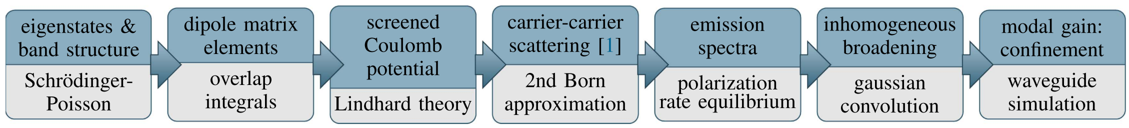

Fig. 2. Flow diagram of gain simulations.

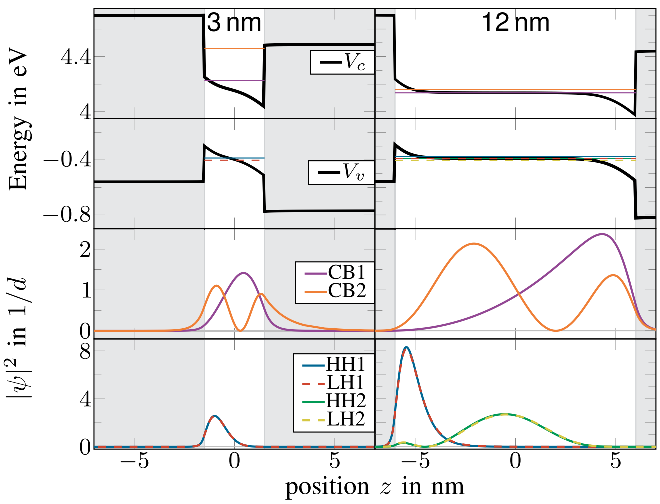

Fig. 3. Band diagrams $V_{c,v}(z)$ and eigenstates (wavefunctions and energies of ground and 1st excited states, if existent) for 3 nm and 12 nm QW, using $p_{\text{eff}} = 50\%$.

a factor p_{eff} which depends on operation mode (electrical [21], [22], [23] vs. optical pumping [20], [24]).

As we use single QWs, the boundary conditions for the electric potential are assumed as an infinite barrier setup [20] corresponding to Neumann boundary conditions at infinity.

While simpler models only consider direct transitions between bands through dipole elements, we also take Coulomb interaction and the resulting scattering into account, which is essential for the high carrier density regime that UV laser diodes operate in [26]. The combination of both interactions establishes an equilibrium which allows to calculate gain, with the scattering leading to homogeneous broadening, bandgap renormalization, and excitonic gain enhancement.

Random alloy fluctuations lead to both hole localization effects and bandgap fluctuations [27]. Neglecting the former, we can consider the variation in the bandgap through a normal distribution of band energies [28], which in turn leads to inhomogeneous broadening (IHB) of the gain spectrum. We approximate the spectral IHB through Gaussian convolution with parameter σ_{IHB}.

σ_{IHB} is calibrated by a non-linear least squares fit, which matches the convolution of simulated spectra with Gaussian broadening against measurements taken with optical pumping (see Section III). However, application in laser diodes relies on electrical pumping. Therefore, we also simulate spectra for this operation mode, using the same σ_{IHB}.

The optical confinement factors to convert material gain to modal gain were obtained from 1D waveguide simulations using SiLENSe [29] and are computed as $\Gamma_{3\text{ nm}} = 1.3\%$ and $\Gamma_{12\text{ nm}} = 8.4\%$ respectively.

III. Comparison to Experiment

Experimental net gain spectra of the structures were measured with the variable stripe length method (VSLM) using non-resonant optical pumping by a 193 nm ArF laser [30]. The measurements were subject to internal losses of about 10/cm which have been deducted to allow comparison with simulated modal gain spectra (Fig. 4). We limit the fitting range for the IHB parameter σ_{IHB} to the high-energy edge and peak (see Fig. 4). The low-energy edge (Urbach tail) is excluded as our model cannot accurately predict it.

For optical pumping above the barrier energy, carriers generated in the barriers by the pump laser screen most of the polarization charges. Both previous and current alignments between experimental and simulated spectra indicate $p_{\text{eff}} \approx 10\%$. We also assume that the average electron density n and hole density p in the QW are equal.

Calculating all confined states in the 12 nm QW, we obtain $N_{\text{vb}} = 20$ valence subbands and $N_{\text{cb}} = 7$ conduction subbands, which are included in the gain calculation.

Both experiment and simulation show dominant TE emission.

We see that for similar optical excitation power density P, the 3 nm and 12 nm QW show very different carrier densities and spectra, with the wide QW providing higher peak gain.

The 3 nm QW shows a broader spectral width compared to the 12 nm QW even without IHB, and additionally requires more IHB to match the width of the experimental spectra, with $\sigma_{\text{IHB, 3 nm}} = 40(20)$meV vs. $\sigma_{\text{IHB, 12 nm}} = 19(4)$meV.

IV. Analysis of Gain

The different spectral width between 3 nm and 12 nm QW can be understood with a simple variational approach to the bands $E^n_{c,v}(k_r) = \frac{\hbar^2}{2m^*}\left[\left(\frac{n\,\pi}{d_{\text{QW}}}\right)^2 + k_r^2\right]$ of an infinite QW, with effective mass m^* of the respective charge carriers:

- Large QW widths d_{QW} lead to small subband spacing in E^n_c (compare Fig. 3). The higher density of states reduces quasi Fermi level splitting and thus energy spread: high energy states are depopulated and therefore generate no gain, leading to a sharper spectrum independently of IHB.
- Localized landscape theory predicts an energy landscape with a spread of energetically favorable quantum dot-like states [27]. If we treat their uneven distribution as a variation of d_{QW} of the envelope QW, then $\Delta E^n_v \propto d_{\text{QW}}^{-3} \Delta d_{\text{QW}}$. As such, wide QWs have their bands broadened less and show a lower σ_{IHB} which matches the behavior of the fit parameters noted in Fig. 4.

From the 12 nm QW gain characteristic in Fig. 6, we extrapolate a transparency density of $n_{\text{tr}} = 16.4 \cdot 10^{18}$ cm^2 and a differential gain of $\partial G = 18.7 \cdot 10^{18}$ cm^2. This

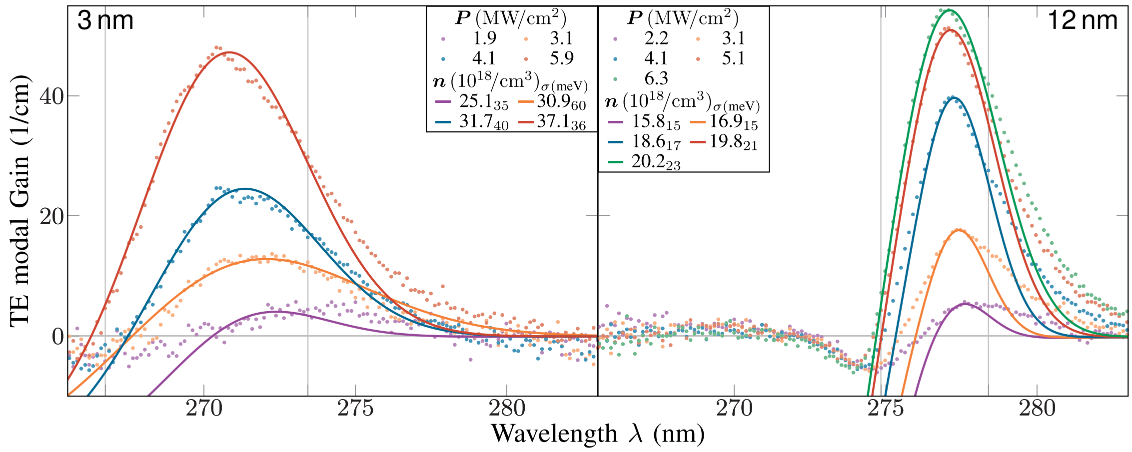

Fig. 4. Measured [25] (dots) versus simulated (lines) modal gain spectra for optical pumping in 3 nm and 12 nm QW lasers, at different optical excitation power densities P or charge densities $n = p$ respectively. λ range for IHB fit σ denoted by gray lines.

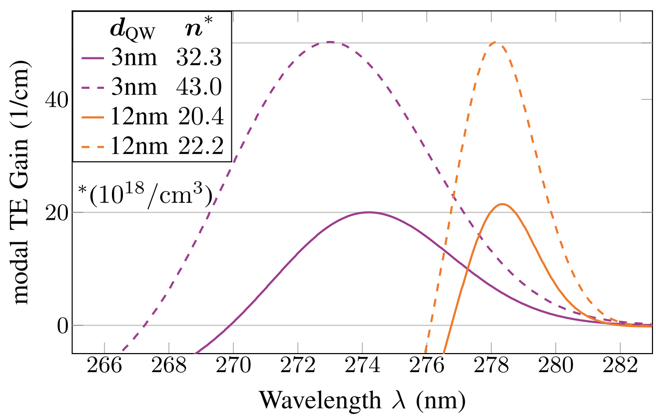

Fig. 5. Simulated gain spectra $G(\lambda)$ with IHB for 50% screening in 3 nm and 12 nm QW lasers.

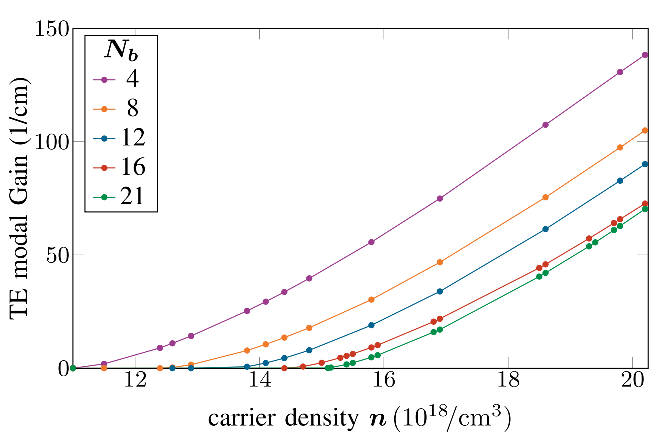

Fig. 6. Peak gain for 12 nm QW and different band cutoffs N_b, with IHB from experimental fit (using all $N_b = 21$ bands).

suggests a notable advantage over the characteristics $n_{\text{tr}} = 24.9 \cdot 10^{18}$ cm^3, $\partial G = 3.6 \cdot 10^{18}$ cm^2 of the 3 nm QW, as the wide QW achieves more gain at lower carrier densities.

Extending the measurements and simulations to $d_{\text{QW}} \in \{3, 6, 9, 12\}$ nm [25] indicates that

- $\sigma_{\text{IHB}}(d_{\text{QW}})$ sharply drops below 6 nm, then flattens out.
- $\partial G(d_{\text{QW}})$ increases slightly better than linearly.
- $n_{\text{tr}}(d_{\text{QW}})$ sharply drops below 6 nm, then declines linearly.

A multi-QW design could combine four 3 nm QWs to reach the same overall active volume and therefore 2D density. As such, an argument can be made to compare the characteristics with respect to 2D carrier density. As multi-QWs cannot lower the transparency density, we merely convert to 2D differential gain $\partial G_{\text{2D, 3 nm}} = 1.2 \cdot 10^{-11}$ cm and $\partial G_{\text{2D, 12 nm}} = 1.6 \cdot 10^{-11}$ cm respectively. We see that a single 12 nm QW is still preferable.

V. Electrical Pumping

For electrical pumping, we assume $p_{\text{eff}} = 50\%$ and, due to lack of further data, $n = p$. As such, only p_{eff} is changed between the simulations for optical versus electrical pumping.

The simulated gain spectra for $p_{\text{eff}} = 50\%$ in Fig. 5 show similar behavior to what we observed for optical pumping, though with a stronger redshift towards lower charge densities as well as a higher transparency density. Both of these effects are explained by the quantum-confined Stark effect: The distorted potential decreases both subband level distance and wavefunction overlap at low n, p where polarization charges cannot be compensated with free charges.

The 12 nm QW requires notably lower carrier density to achieve the same peak gain. The differential gain $\partial G_{\text{3nm}} = 2.8 \cdot 10^{18}$ cm^2 and $\partial G_{\text{12nm}} = 15.8 \cdot 10^{18}$ cm^2 is lower compared to $p_{\text{eff}} = 10\%$. The 12 nm QW retains its relative advantage, as screening is supplied by low energy states. This holds even in comparison with a 3 nm multi-QW setup.

VI. Band Cutoff

Wide QWs possess a much larger number of valence subbands N_{vb} and conduction subbands N_{cb}, with Coulomb interactions arising between all of them. As a result, computational effort is

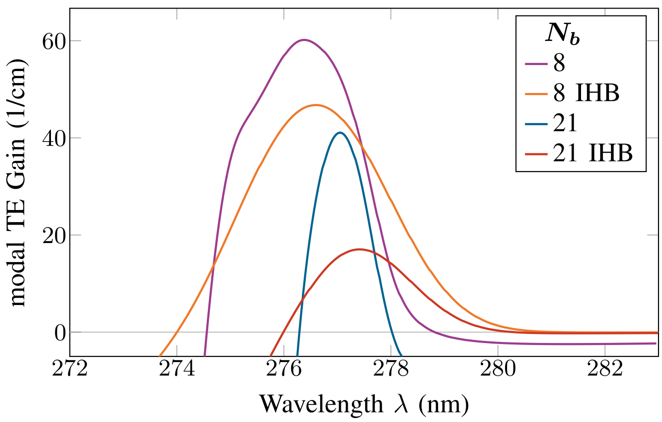

Fig. 7. Simulated gain spectra for a 12 nm QW with $n = 16.9 \cdot 10^{18}$ cm^2 and 90% screening ($p_{\text{eff}} = 10\%$), with and without IHB.

dominated by taking scattering into account, extending simulation time by orders of magnitude. This is typically compensated for by limiting N_{vb} and N_{cb} in the simulation, as complexity scales with $(N_{\text{vb}} + N_{\text{cb}})^4$ and higher-energy bands are assumed to have less impact on the spectrum. We investigate the impact of said bands quantitatively.

This is of particular interest for wide QWs, as far more bound states exist, in contrast to e.g. the 3 nm QW which only possesses $N_{\text{vb}} = 4, N_{\text{cb}} = 2$ confined bands.

For simulations of the 12 nm QW under optical pumping ($p_{\text{eff}} = 10\%$), the full number of bands is $N_{\text{vb}} = 20, N_{\text{cb}} = 7$. N_{vb} is higher by a factor of 3 due to 6-band $k \cdot p$. We compare gain spectra where a limit N_b with $N_{\text{vb}} \leq N_b,\ N_{\text{cb}} \leq \max(\frac{1}{3}N_b, 3)$ is imposed on the bands, the results of which are plotted in Figs. 6 and 7. Note that $N_b = 21$ represents the regular simulation that considers all bands.

As can be seen in Fig. 6, while the differential gain ∂G is only marginally affected by N_b, considering more (or all) bands leads to a sharp increase in transparency density. For a fixed frequency, taking more bands into account increases the density of states, which shifts the quasi Fermi levels such that occupation of higher states is reduced. The unoccupied states contribute absorptively, thereby reducing gain.

As such, we observe that for low N_b peak gain is drastically overestimated, with $N_b = 4$ being roughly $\Delta G = 60 + -10/$ cm above the unlimited simulation. Even the $N_b = 16$ case is off by $\Delta G = 3.8 + -1.4/\text{cm}$, which may not seem much, but still distorts the behavior near threshold.

Fig. 7 shows select spectra of a 12 nm QW for fixed charge densities, with/without IHB of $\sigma_{\text{IHB}} = 18$ meV. The spectra with IHB display that the higher-energy bands both reduce amplitude and increase wavelength of peak gain. The difference stands out even more for the spectra without IHB, as the shape of the gain peak isn't smoothed out – for $N_b = 8$ we see two distinct transitions, one of which is absorbed entirely when higher-energy bands are included. We infer that higher-energy bands affect the height, width and shape of the gain peak. Inclusion of all bands is thus required to obtain a proper fit to experimental data.

For simulations with electrical pumping ($p_{\text{eff}} = 50\%$), all these considerations are heavily amplified. Higher subbands are even more crucial as the ground states exhibit a low wavefunction overlap. Choosing $n, p = 18.9 \cdot 10^{18}$ cm^3 such that $G = 5$ cm, we find $N_{\text{cb}} = 6, N_{\text{vb}} = 9$ bands. Analyzing the contributions of different transitions to peak gain, the ground state transitions provide no gain (their own transition energy being too far below that of the peak), the bands within $N_b = 4$ only explain 52% of gain, and the higher-energy bands are essential to correctly simulate gain. Some transitions with bands beyond $N_b = 4$ provide the remaining 48% of peak gain, while others are absorptive. This is consistent with Fig. 3 and previous findings [20], [31] which show the ground state's screening effect causing gain to rely on excited states. As these investigations were limited to few bands, the major impact of high-energy bands constitutes a new insight.

VII. Conclusion

We present a theory of gain for AlGaN QWs that matches experimental results. Our simulations explain measured gain spectra for optically pumped QW lasers emitting at 275 nm, for multiple charge densities and QW widths. We break down which transitions contribute to gain. These findings are applied to electrically pumped QWs. Through that, we confirm previous reports [20] that wide QWs are preferable for UV-C lasers and that gain in wide QWs mainly originates from excited states.

It is shown that IHB has a larger impact on narrow wells. For wide QWs, we find that higher-energy bands have a notable impact on the gain spectra, both in terms of peak gain and spectral width. Their overall absorptive contribution is analyzed quantitatively and determined to be significant.

References

[1] W. Chow and S. Koch, *Semiconductor-Laser Fundamentals: Physics of the Gain Materials*. Berlin, Germany: Springer, 2013.

[2] Z. Zhang et al., "Key temperature-dependent characteristics of AlGaN-based UV-C laser diode and demonstration of room-temperature continuous-wave lasing," *Appl. Phys. Lett.*, vol. 121, no. 22, Nov. 2022, Art. no. 222103, doi: 10.1063/5.0124480.

[3] Z. Zhang et al., "Design and characterization of a low-optical-loss UV-C laser diode," *Japanese J. Appl. Phys.*, vol. 59, no. 9, Aug. 2020, Art. no. 094001, doi: 10.35848/1347-4065/abaac6.

[4] K. Sato et al., "Analysis of carrier injection efficiency of AlGaN UV-B laser diodes based on the relationship between threshold current density and cavity length," *Japanese J. Appl. Phys.*, vol. 60, no. 7, Jun. 2021, Art. no. 074002, doi: 10.35848/1347-4065/ac0643.

[5] F. Römer et al., "Carrier transport in a deep ultraviolet mixed quantum well light emitting diode," *IEEE Photon. J.*, vol. 16, no. 1, Feb. 2024, Art. no. 8200106, doi: 10.1109/JPHOT.2024.3351965.

[6] B. Witzigmann et al., "Analysis of substrate modes in GaN/InGaN lasers," *Proc. SPIE*, vol. 6468, pp. 197–204, 2007, doi: 10.1117/12.700920.

[7] E. Illy, M. Knowles, E. Gu, and M. Dawson, "Impact of laser scribing for efficient device separation of led components," *Appl. Surf. Sci.*, vol. 249, no. 1, pp. 354–361, 2005, doi: 10.1016/j.apsusc.2004.12.033.

[8] A. Hohnholz et al., "Multimaterial bathless stereolithography using aerosol jet printing and UV laser based polymerization," *J. Laser Appl.*, vol. 31, no. 2, Apr. 2019, Art. no. 022301, doi: 10.2351/1.5096106.

[9] S. A. Asher, *Ultraviolet Raman Spectrometry*. Chichester, U.K.: Wiley, 2002, doi: 10.1002/0470027320.s0408.

[10] E. Gutmann, F. Erfurth, A. Drewitz, A. Scheibe, and M. C. Meinke, *UV Fluorescence Detection and Spectroscopy in Chemistry and Life Sciences*. Cham, Switzerland: Springer, 2016, pp. 351–386.

[11] J. Piprek, Ed., *Nitride Semiconductor Devices: Principles and Simulation*. Weinheim, Germany: Wiley, 2007.

[12] Q. Yan, P. Rinke, M. Scheffler, and C. G. Van de Walle, “Strain effects in group-III nitrides: Deformation potentials for AlN, GaN, and InN,” *Appl. Phys. Lett.*, vol. 95, no. 12, Sep. 2009, Art. no. 121111, doi: 10.1063/1.3236533.

[13] M. Feneberg et al., “Anisotropic absorption and emission of bulk $(1\bar{1}00)$ AlN,” *Phys. Rev. B*, vol. 87, Jun. 2013, Art. no. 235209, doi: 10.1103/PhysRevB.87.235209.

[14] M. Feneberg et al., “Band gap renormalization and Burstein–Moss effect in silicon- and germanium-doped wurtzite GaN up to 10^{20}cm^{-3},” *Phys. Rev. B*, vol. 90, Aug. 2014, Art. no. 075203, doi: 10.1103/PhysRevB.90.075203.

[15] Z. Li et al., “Plasma assisted molecular beam epitaxy growth mechanism of AlGaN epilayers and strain relaxation on AlN templates,” *Japanese J. Appl. Phys.*, vol. 60, no. 7, Jun. 2021, Art. no. 075504, doi: 10.35848/1347-4065/ac0bed.

[16] V. Jmerik et al., “AlGaN quantum well structures for deep-UV LEDs grown by plasma-assisted MBE using sub-monolayer digital-alloying technique,” *J. Cryst. Growth*, vol. 311, pp. 2080–2083, Mar. 2009, doi: 10.1016/j.jcrysgro.2008.11.080.

[17] S. L. Chuang and C. S. Chang, “Effective-mass Hamiltonian for strained wurtzite GaN and analytical solutions,” *Appl. Phys. Lett.*, vol. 68, no. 12, pp. 1657–1659, Mar. 1996, doi: 10.1063/1.115896.

[18] L. Uhlig, J. Tepaß, M. Hajdel, G. Muziol, and U. T. Schwarz, “Transition between quantum confinement and bulklike behavior in polar quantum wells,” *Phys. Rev. B*, vol. 108, Jul. 2023, Art. no. 045304, doi: 10.1103/PhysRevB.108.045304.

[19] O. Ambacher et al., “Two dimensional electron gases induced by spontaneous and piezoelectric polarization in undoped and doped AlGaN/GaN heterostructures,” *J. Appl. Phys.*, vol. 87, no. 1, pp. 334–344, Jan. 2000, doi: 10.1063/1.371866.

[20] B. Witzigmann, F. Römer, M. Martens, C. Kuhn, T. Wernicke, and M. Kneissl, “Calculation of optical gain in AlGaN quantum wells for ultraviolet emission,” *AIP Adv.*, vol. 10, no. 9, Sep. 2020, Art. no. 095307, doi: 10.1063/5.0021890.

[21] J. Piprek and S. Li, “Electron leakage effects on GaN-based light-emitting diodes,” *Opt. Quantum Electron.*, vol. 42, no. 2, pp. 89–95, Jan. 2010, doi: 10.1007/s11082-011-9437-z.

[22] C. A. Flory and G. Hasnain, “Modeling of GaN optoelectronic devices and strain-induced piezoelectric effects,” *IEEE J. Quantum Electron.*, vol. 37, no. 2, pp. 244–253, Feb. 2001, doi: 10.1109/3.903075.

[23] R. R. Aguileta-Vazquez et al., “Polarization-matching and carrier confinement in III-nitride deep-ultraviolet light-emitting diodes,” *J. Appl. Phys.*, vol. 134, no. 18, Nov. 2023, Art. no. 184501, doi: 10.1063/5.0166175.

[24] S. F. Chichibu et al., “Effective band gap inhomogeneity and piezoelectric field in InGaN/GaN multiquantum well structures,” *Appl. Phys. Lett.*, vol. 73, no. 14, pp. 2006–2008, Oct. 1998, doi: 10.1063/1.122350.

[25] G. Cardinali et al., “Gain characteristics of optically-pumped UVC lasers with wide AlGaN single-quantum-well active regions,” *Physica Status Solidi (a)*, p. 2400067, 2024, doi: 10.1002/pssa.202400067.

[26] J. Moloney, J. Hader, and S. Koch, “Quantum design of semiconductor active materials: Laser and amplifier applications,” *Laser Photon. Rev.*, vol. 1, no. 1, pp. 24–43, 2007, doi: 10.1002/lpor.200610003.

[27] R. Finn and S. Schulz, “Impact of random alloy fluctuations on the electronic and optical properties of (Al,Ga)N quantum wells: Insights from tight-binding calculations,” *J. Chem. Phys.*, vol. 157, no. 24, Dec. 2022, Art. no. 244705, doi: 10.1063/5.0132490.

[28] F. Römer, M. Guttmann, T. Wernicke, M. Kneissl, and B. Witzigmann, “Effect of inhomogeneous broadening in ultraviolet III-Nitride light-emitting diodes,” *Materials*, vol. 14, no. 24, 2021, Art. no. 7890, doi: 10.3390/ma14247890.

[29] STR Group, “SiLENSe–software tool for light emitting diode (LED) bandgap engineering,” 2023. [Online]. Available: https://str-soft.com/devices/silense/

[30] M. Martens et al., “The effects of magnesium doping on the modal loss in AlGaN-based deep UV lasers,” *Appl. Phys. Lett.*, vol. 110, no. 8, Feb. 2017, Art. no. 081103, doi: 10.1063/1.4977029.

[31] G. Muziol et al., “Beyond quantum efficiency limitations originating from the piezoelectric polarization in light-emitting devices,” *ACS Photon.*, vol. 6, no. 8, pp. 1963–1971, 2019, doi: 10.1021/acsphotonics.9b00327.